

PLANETESIMAL ACCRETION AT SHORT ORBITAL PERIODS

SPENCER C. WALLACE¹ AND THOMAS R. QUINN¹

¹*Astronomy Department, University of Washington, Seattle, WA 98195*

ABSTRACT

Formation models in which terrestrial bodies grow via the pairwise accretion of planetesimals have been reasonably successful at reproducing the general properties of the solar system, including small body populations. However, planetesimal accretion has not yet been fully explored in the context of more exotic terrestrial systems, particularly those that host short-period planets. In this work, we use direct N-body simulations to explore and understand the growth of planetary embryos from planetesimals in disks extending down to $\simeq 1$ day orbital periods. We show that planetesimal accretion becomes nearly 100 percent efficient at short orbital periods, leading to embryo masses that are roughly twice as large as the classical isolation mass. For rocky bodies, the physical size of the object begins to occupy a significant fraction of its Hill sphere at orbital periods less than about 50 days. In this regime, most close encounters result in collisions, rather than scattering, and the system cannot bifurcate into a collection of dynamically hot planetesimals and dynamically cold oligarchs, like is seen in previous work. The highly efficient accretion seen at short orbital periods implies that systems of tightly-packed inner planets should be almost completely devoid of any residual small bodies. We demonstrate the robustness of our results to assumptions about the initial disk model, and also investigate how far material can radially mix across the accretion boundary.

1. INTRODUCTION

Planetesimal accretion is one of a number of stages in which micron-sized solids from the protostellar nebula coalesce to eventually build terrestrial planets. In the earliest stages, aerodynamic forces dominate the growth and evolution of the solids. Millimeter-sized bodies grow through adhesive pairwise collisions and stay well-coupled to the surrounding gas. Beyond this size, however, a number of growth barriers present themselves. Most notably, larger solids orbit the central star at Keplerian speeds as they decouple from the gas, which orbits at a sub-keplerian speed due to radial pressure support. This leads the solids to feel a headwind, which is maximally effective at sapping away angular momentum for objects around 1 meter in size. At this size, the timescale for the growing solids to fall onto the star is catastrophically short and leads to what is known as the drift barrier. In addition, two-body collisions between mm- to cm-sized bodies tend to result in bouncing or destruction, rather than continued growth. For these reasons, a number of mechanisms have been proposed which facilitate fast growth from mm to km sizes by locally concentrating solids. Dust traps, streaming instability, pebble piles...etc.

Beyond kilometer scales, gravity begins to dominate and aerodynamic gas drag plays a smaller and smaller role. During this phase, collision cross sections are en-

hanced as gravitational focusing (Safronov 1969) acts to bend the trajectories of bodies undergoing close encounters. Large bodies are most effective at focusing the trajectories of nearby planetesimals, leading to a period of runaway growth (Wetherill & Stewart 1989; Kokubo & Ida 1996; Barnes et al. 2009). Eventually, the largest bodies (known as oligarchs) dynamically heat the surrounding planetesimals, severely limiting further growth (Kokubo & Ida 1998). The end result of this phase is a bimodal population of dynamically cold oligarchs, surrounded by dynamically hot, difficult to accrete residual planetesimals. Lines of evidence suggest that the asteroid belt, kuiper belt and the oort cloud are largely composed of the leftovers of this stage of planet formation. (Mention more specific evidence, morbidelli 09 paper, CAIs?)

Although gas drag has a minimal influence on the Moon to Mars-sized oligarchs, it is enough to prevent these largest bodies from perturbing each other onto crossing orbits. Simulations show that evaporation of the gas disk is required to allow instability to trigger a phase of giant impacts (Mention that disk fraction decay timescale roughly matches timing of giant impacts in SS). It is during this phase that oligarchs collide to form Earth-sized planets (Chambers & Wetherill 1998; Raymond et al. 2006).

Over the last few decades, terrestrial planet formation models have largely advanced by matching properties of

the solar system. Compared to exoplanetary systems, the solar system provides a rich set of constraints (isotopic ratios, cratering records, small body populations) that are mostly unmeasurable for even the closest neighboring planet forming systems. However, the system architectures discovered by spaced-based missions in the last decade reveal that the solar system could very well be an outlier in terms of what a typical planet-forming disk produces. In addition, the sizes and compositions of the terrestrial planets likely rely on a series of finely-tuned events to play out that involve truncation of the primordial planetesimal disk (Raymond & Izidoro 2017), inward, followed by outward migration of an outer giant planet (Walsh et al. 2011), or a large-scale instability triggered by a pair of convergently migrating giant planets (Tsiganis et al. 2005; Levison et al. 2011; Nesvorný 2011). Given qualitatively similar initial conditions, solar system formation models can even occasionally reproduce the correct masses and orbital periods of the terrestrial planets without invoking any of the aforementioned scenarios, given the right random number seed (Fischer & Ciesla 2014).

Given the difficult question of whether to treat the solar system as an outlier, the best way forward is to use statistical samples of exoplanetary architectures to develop and inform formation models. This is generally done through the use of population synthesis models (Ida & Lin 2004; Alibert et al. 2011), but many of the mechanisms in these models are informed and tuned by solar system constraints. One pervasive and exotic result revealed by the Kepler space telescope has the discovery of hundreds of compact multi-planet terrestrial systems, dubbed systems of tightly-packed inner planets (STIPs). Although there is no formal definition of a STIP, they typically contain 3 or more Earth-sized planets with orbital periods extending between 1 and 100 days. Reconciling the structural differences between the solar system (devoid of large bodies interior to 88 days) and STIPs is going to be an important step in building a general, widely-applicable planet formation model.

To date, a large body of work exists that has attempted to reproduce the architectures of STIPs, starting from planetary embryos (cite some examples). However, the runaway and oligarchic growth phases, which precede the assembly of the embryos, are assumed to be ubiquitous. Given that the timescales for accretion and gravitational scattering scale differently with encounter velocity, which itself scales with orbital period, it is not entirely clear that planetary embryos should form in the same way close to the star as they do at much longer, more thoroughly studied orbital periods. In this paper, we use direct N-body simulations to explore the

outcome of the planetesimal accretion stage at orbital periods shorter than 100 days. In particular, we seek to understand what the orbital and mass distributions of the embryos and residual planetesimals look like, and to assess whether the initial conditions used by late-stage simulations of STIP assembly are reasonable.

In section 2 we provide an overview of the theory behind planetesimal accretion and show that assumptions used to derive the well-known modes of growth are only valid at sufficiently long orbital periods. We then motivate the need for N-body simulations to study this problem and describe the code used, along with how our initial conditions were constructed in section 3. In section ??, we present parameter study of planetesimal accretion using a series of simulations of narrow annuli at various orbital periods. We also present a set of simulations starting with a much wider planetesimal disk and demonstrate that a transition between accretion modes occurs at moderately small ($\simeq 50$ d) orbital periods. Next, we assess the impact of simplifications made to our collision model on this result in section 6. In section 7, we discuss the implications of this multimodal accretion behavior throughout the disk for planet formation models and conclude.

2. OVERVIEW OF PLANETESIMAL ACCRETION

2.1. Oligarchic and Runaway Growth

We begin our analysis by considering a disk of equal planetesimals with radius r_{pl} , mass m_{pl} and surface density Σ_{pl} . The collision rate in the vicinity of an orbit defined by Keplerian frequency Ω can be written as $n\Gamma v$, where $n = \Sigma_{pl}\Omega/2m_{pl}v$, Γ is the effective collision cross section and v is the typical encounter velocity between planetesimals. Assuming that every collision results in a perfect merger, the growth rate of a planetesimal is given by

$$\frac{dM}{dt} = \frac{\Sigma\Omega}{2m_{pl}}\Gamma. \quad (1)$$

In the case where the collision cross section Γ depends only on the physical size of the planetesimals, the growth scales linearly with mass and the mass distribution is expected to evolve in an ‘orderly’ fashion. However, bodies larger than ~ 100 km in size are expected to exert a significant gravitational force on each other during encounters and the collision cross section depends on both the size of the bodies and their encounter velocities. In this case, $\Gamma = \Gamma_{geo}(1 + v_{esc}^2/v^2)$, where v_{esc} is the escape velocity from the two bodies at the point of contact.

In the limit that $v_{esc} \gg v$, it can be shown that $M \propto M^{4/3}$, which implies a runaway scenario, in which growth accelerates with mass. This mode of growth was

confirmed with N-body simulations by Kokubo & Ida (1996) and appears necessary to construct protoplanets within the lifetime of a protoplanetary disk. Due to the velocity dependence of the gravitational focusing effect, it isn't clear how ubiquitous this mode of growth is. In particular, encounter velocities at short orbital periods will be rather large (because $v \sim v_k$) and the $v_{esc} \gg v$ condition may not always be satisfied. The effect that a dynamically hot disk has on runaway growth will be examined in detail in section ??.

An important feature is missing from the model described above, which limits its applicability at late times. Encounters between planetesimals that do not result in a collision play a crucial role over long timescales. These close encounters act to convert energy from Keplerian shear into random motion. Over time, this gravitational stirring effect will raise the typical encounter velocities between bodies and diminish the effectiveness of gravitational focusing. With a spectrum of masses, these velocity differences become even more pronounced because as system drifts towards a state of quasi-equilibrium where $v \sim m^{1/2}$. For a system of equal mass bodies in which encounters are driven by random motions rather than Keplerian shear (dispersion dominated), the timescale for gravitational stirring is described by the two-body relaxation time (Ida & Makino 1993)

$$t_{relax} = \frac{v^3}{n\pi G^2 m_{pl} \ln \Lambda}, \quad (2)$$

where $\ln \Lambda$ is the Coulomb logarithm, typically taken to be ≈ 10 for a planetesimal disk. Despite the fact that the behavior of gravitational stirring is well-described by two-body formalism, (Ida & Makino 1993) found that the stirring in a planetesimal disk is actually driven by close encounters. As we will show in section 4, gravitational stirring effectively shuts off when the Hill sphere of a body becomes comparable to its physical size. In this case, close encounters tend to result in collisions, and the main pathway for energy exchange between planetesimals is unable to operate.

As mentioned above, the system will tend toward a state of energy equipartition for a non-uniform mass distribution. Kokubo & Ida (1998) showed that runaway growth is actually self-limiting. As the runaway bodies grow larger, they become more effective at heating the remaining planetesimals, which diminishes the effectiveness of gravitational focusing and throttles the growth rate. Around the time that the massive runaway bodies make up about 50 percent of the solid surface density (citation), a period of less vigorous 'oligarchic' growth commences, in which the few largest bodies continue to accrete planetesimals at similar rates.

The picture described above relies upon an important factor, which is that the mass distribution evolves slow enough for gravitational stirring to maintain energy equipartition. In other words, the relaxation timescale must remain short relative to the growth timescale. For typical conditions near the terrestrial planet forming region of the solar system, this timescale condition is satisfied. Due to the steep dependence of the relaxation time on encounter velocity, this condition can easily be violated at shorter orbital periods.

In figure 1, we show ratio between the relaxation and collision timescale for a population of equal-mass planetesimals as a function of orbital period. Here, the encounter velocity is described by $v = \left(5/8 \langle e^2 \rangle^{1/2} + \langle i^2 \rangle^{1/2}\right)^{1/2} v_k$, where $\langle e^2 \rangle^{1/2}$ and $\langle i^2 \rangle^{1/2}$ are the eccentricity and inclination dispersions of the planetesimal disk and v_k is the Keplerian velocity. For simplicity, we assume that $\langle e^2 \rangle^{1/2} = 2 \langle i^2 \rangle^{1/2}$ (Ida et al. 1993) and that the eccentricity dispersion is constant with orbital period. The eccentricity dispersion is described in units scaled by the Hill factor $(m_{pl}/3M_{star})^{1/3}$ such that $e_h = 1$ corresponds to the boundary between shear and dispersion dominated encounters. The horizontal dashed line indicates where $t_{relax} = t_{coll}$. The timescale criterion for oligarchic growth is only satisfied in regions where the disk is sufficiently dynamically cold and the orbital period is sufficiently long. In section ?? we will explore the behavior and outcome of planetesimal accretion in regions where this criterion is *not* satisfied.

2.2. Planetesimal Size and Extent of Hill Sphere

In the formalism described above, the mass and velocity distribution of the bodies are both a function of time. Due to the interdependence of these quantities, it is not clear whether the timescales for gravitational scattering and growth will remain proportional as the oligarchs develop. In the case of many studies of planetesimal accretion in the solar system (cite examples), the $t_{relax} \ll t_{coll}$ condition must remain true, otherwise runaway growth would have continued until all of the planetesimals were consumed. However, it isn't immediately clear what will happen if the system begins in a state where $t_{coll} \ll t_{relax}$.

An insight into the expected behavior in this regime can be gained by defining the dimensionless parameter α , which is the ratio between the physical size of a body and it's Hill radius

$$\alpha = \frac{r_{pl}}{r_h} = \frac{1}{a} \left(\frac{9M_*}{4\pi\rho_{pl}} \right)^{1/3}, \quad (3)$$

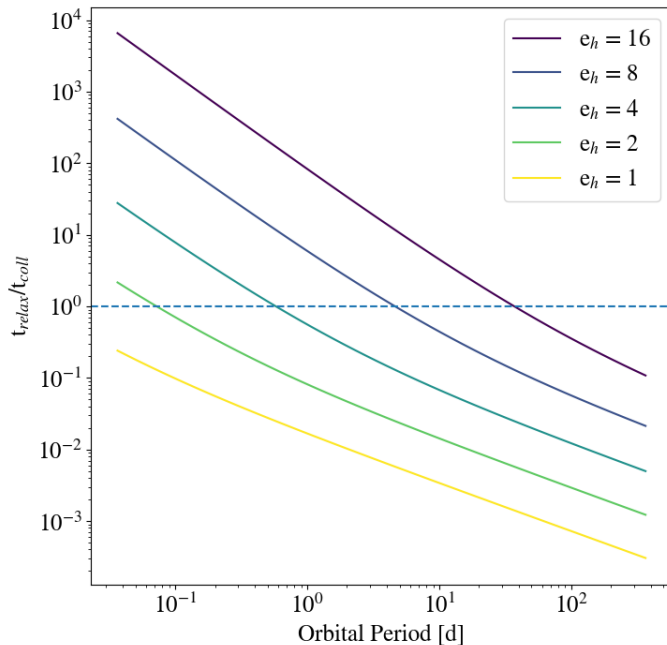


Figure 1. The ratio between the two-body relaxation and collision timescale for a population of equal-mass planetesimals. Only in regions where $t_{\text{relax}} \ll t_{\text{coll}}$ can the velocity distribution respond to changes in the mass of the bodies such that oligarchic growth can operate. This condition is no longer satisfied for a dynamically hot disk at sufficiently short orbital periods.

where a is the semimajor axis of the body and ρ_{pl} is its bulk density. Assuming a fixed bulk density as bodies collide and grow, and that no large-scale migration occurs, the scaling of both r_{pl} and r_h with $m_{\text{pl}}^{1/3}$ means that α will be constant with time. For a composition of ice and rock, α is small for any populated region of the solar system ($\alpha \sim 10^{-2}$ for Earth and $\alpha \sim 10^{-4}$ in the Kuiper belt). As one moves close to the star α becomes larger than 1, which implies that the physical extent of a body exceeds its Hill sphere. (also mention that hill sphere size independent of velocity for small eccentricity)

The size of α controls the relative importance of gravitational scattering and collisions in driving the evolution of the planetesimal disk. In the case that α is small, most close encounters will result in a gravitational interaction only, moving the system toward a state of relaxation. If, however, the Hill sphere is largely filled by the body itself, these same encounters will instead drive evolution of the masses. Because α is independent of time, the innermost region of the planetesimal disk, where collisions dominate over scattering events, should remain that way.

We also introduce a second dimensionless quantity, which relates the physical size of the bodies to the velocity state of the system

$$\beta = \frac{r_{\text{pl}}}{r_g}. \quad (4)$$

where $r_g = Gm_{\text{pl}}/v^2$ is the gravitational radius of a body. Encounters between bodies inside of a distance of r_g result in significant deflections of their trajectories. It should be noted that the gravitational focusing enhancement factor v^2/v_{esc}^2 is equal to 1 for $\beta = 1$. In the case where r_g is smaller than the size of a planetesimal, the gravitational focusing enhancement factor will be between 0 and 1.

Need a transition to next section here.

3. NUMERICAL METHODS

We use the tree-based N-body code CHANGA¹ to model the gravitational and collisional evolution of planetesimals at short orbital periods (where α is large). CHANGA is written using the CHARM++ parallel programming language and has been shown to perform well on up to half a million processors (Menon et al. 2015) and can follow the evolution of gravitationally interacting swarms of up to billions of particles. Using a modified Barnes-Hut tree with hexadecapole expansions of the moments to approximate forces, CHANGA integrates the equations of motion using a kick-drift-kick leapfrog scheme. For all of the simulations presented in this paper, we use a node opening criteria of $\theta_{\text{BH}} = 0.7$. Additional information about the code is available in (Jetley et al. 2008).

Using the neighbor-finding algorithm in CHANGA, originally designed for SPH calculations, we have recently implemented a solid body collision module in the code. This work is largely based on the solid-body collision implementation in PKDGRAV, which is described in Richardson (1994) and Richardson et al. (2000). To summarize, imminent collisions are detected during the ‘drift’ phase by extrapolating positions of bodies forward in time, using the velocity calculated at the opening ‘kick’. For each body, any neighboring particles which fall within a search ball of radius $fillinlater$ are tested for an imminent collision. In the case that a collision is detected, the particles are merged into a single larger body, which is given the center of mass position and velocity of the two children. Resolving a collision can produce another imminent collision, so collisions are handled one-by-one and another full collision check is run

¹ A public version of CHANGA can be downloaded from <http://www-hpcc.astro.washington.edu/tools/ChaNGa.html>

after the previous event is resolved. For a more detailed description of the collision module in CHANGA, see (Wallace & Quinn 2019). (mention grav stepping here as well, since its used for all simulations)

4. NARROW ANNULUS SIMULATIONS

We begin by presenting a parameter study of planetesimal accretion, motivated by two questions raised in section 2. 1. Does runaway growth still operate when the condition that $v \ll v_{esc}$ is not satisfied? 2. How does planetesimal accretion proceed when the planetesimals themselves occupy a significant fraction of their Hill spheres?

To answer these questions, we run a series of simulations in which a narrow annulus of planetesimals orbits a star. The values of α and β are varied individually. 4000 planetesimals with individual masses of 5×10^{23} g are placed with semimajor axes randomly drawn between 0.95 and 1.05 AU about a $1 M_{\odot}$ star. The argument of perihelion ω , longitude of ascending node Ω , and mean anomaly M for each body is drawn from a uniform distribution $\in [0, 2\pi)$. The inclination dispersion $\langle i^2 \rangle^{1/2}$ is chosen to be half the eccentricity dispersion $\langle e^2 \rangle^{1/2}$ (Ida et al. 1993).

In the ‘nominal’ case, we give the bodies a bulk density of 3 g cm^{-3} , and $\langle e^2 \rangle^{1/2} = 4e_h$, where $e_h = ea/r_h$ (define this in the previous section instead) which corresponds to $\alpha = 3.6 \times 10^{-2}$ and $\beta = 3.4 \times 10^{-3}$. These parameters are chosen to match the initial conditions of Kokubo & Ida (1998), which gave rise to oligarchic growth. To vary the value of α , we alter the bulk density of the particles. In the high- α case, the bulk density is reduced by a factor of ~ 7100 , which produces $\alpha = 1$. To vary β , the eccentricity dispersion is increased. For the high- β case, $\langle e^2 \rangle^{1/2}$ is increased to $1500e_h$, which corresponds to $\beta = 15,000$.

In all cases, the simulations are evolved with a base timestep of 1.7 days, which corresponds to 3% of an orbital dynamical time $\sqrt{a^3/GM_*}$. Due to the vastly differing growth timescales in each case, a simulation is stopped when the growth of the most massive body flattens out. In figure 2, we show the a-e distribution of bodies in the initial (blue) and final (orange) snapshots from each of the 4 simulations. The size of the points indicates the relative masses of the bodies. Only in the case of small α does a residual population of dynamically hot planetesimals develop. The lack of high eccentricity planetesimals in the large α case suggests that most encounters instead result in accretion. In the case of large β , the protoplanets and remaining planetesimals end up in a dynamically cool state, compared to the initial con-

ditions. (Are the inelastic collisions playing a significant role here?)

In figure 3, we show the mass distribution of bodies from the final snapshot in each of the four cases. In addition to leaving fewer residual planetesimals, the large α simulations produce significantly larger embryos. Despite the vastly different encounter velocities of each population of bodies, the initial size of β (so long as bodies remain in the dispersion-dominated regime) appears to have no significant effect on the final distribution of masses.

To investigate whether any of these planetesimal disks underwent runaway growth, we examine the time evolution of the maximum and mean masses in each case. The ratio $m_{max}/\langle m \rangle$ is plotted in figure 4. On this plot, a positive slope indicates that the growth rate is accelerating with mass, which is evident in all four cases. Even with a large value of β , which means that the effective collision cross section is very near the geometric value, runaway growth still appears to operate. This seems to imply that, as bodies collide and grow, the relative increase in their gravitational focusing factors, rather than its absolute size, is what drives the system towards runaway growth. Although larger encounter velocities will lengthen the growth timescales, this mode of growth appears to be inevitable, so long as gravity is the dominant force in the system.

Additionally, these results suggest that the value of α , which is a function of only the initial conditions, controls the qualitative outcome of accretion. Across most of a planet-forming disk, α is small, and frequent gravitational encounters between the growing bodies will allow oligarchic growth to operate. In the dispersion-dominated regime, close encounters drive the stirring between planetesimals and embryos (Weidenschilling 1989; Ida 1990). When α is large, the Hill sphere of a body is no longer mostly empty space, and close encounters that would otherwise result in stirring instead result in accretion. In this regime, we observe that runaway growth still commences, but nearly all of the planetesimals are swept up by the forming protoplanets, rather than being scattered onto higher eccentricity orbits, where they would otherwise remain as a remnant of the early stages of planet formation (Kokubo & Ida 1998, 2000).

5. FULL DISK SIMULATION

5.1. Initial Conditions

Motivated by the apparent dependence of accretion modes on α , we next investigate whether this highly efficient, non-oligarchic growth mode should be expected to operate in a typical planet-forming disk. Given the dearth of short period terrestrial planets observed

Table 1. Summary of Full Disk Simulations Run

Name	m_{pl}^a	N_{pl}^b	A^c	α^d
fdHi	5×10^{22}	903,687	100	1.5
fdHiShallow	5×10^{22}	903,687	100	0.5
fdHiSteep	5×10^{22}	903,687	100	2.5
fdLo	1×10^{22}	45,185	1	1.5

NOTE

^a Planetesimal mass [g]^b Number of planetesimals^c Solid surface density normalization (relative to MMSN)^d Solid surface density power law index

around M stars (citation), we model a series of wide planetesimal disks, which span from 1 to 100 days in orbital period orbiting a late-type M star of mass $0.08 M_\odot$. For a population of planetesimals with a bulk density of 3 g cm^{-3} , this orbital period range corresponds to $\alpha \in (0.7, 0.05)$. By simultaneously modeling a broad range of orbital periods, we can determine the critical value of α that divides these two modes of accretion, and also explore how the oligarchic/non-oligarchic accretion boundary affects the resulting distribution of protoplanets.

Four wide disk simulations are run in total (see table 1). In each case, the solid surface density follows a power law profile

$$\Sigma(r) = \left(\frac{M_*}{M_\odot} \right) A \Sigma_{mmsn} \left(\frac{r}{1 \text{ AU}} \right)^{-\alpha}, \quad (5)$$

where M_* is the mass of the central star, $\Sigma_{MMSN} = 10 \text{ g cm}^{-2}$ is surface density of the minimum-mass solar nebula (Hayashi 1981) at 1 AU, and A is an enhancement factor. In the first case (fdHi), we model a disk that follows a MMSN power law slope, with the overall normalization enhanced by a factor of 100. This choice of parameters for the solid surface density profile appears necessary in order to reproduce many observed short period terrestrial worlds in-situ (Hansen & Murray 2012). Additionally, we vary the power law index (fdHiShallow, fdHiSteep) and overall normalization (fdLo) of the solids profile.

In all cases, the eccentricities and inclinations of the bodies are randomly drawn from a Rayleigh distribution, with $\langle e^2 \rangle^{1/2} = 2 \langle i^2 \rangle^{1/2} = e_{eq}$. The value of e_{eq} is chosen such that the timescales for viscous stirring and aerodynamic gas drag on the planetesimals are in equilibrium. The viscous stirring timescale is given by Ida & Makino (1993) as

$$\tau_{vs} = \frac{\langle e^2 \rangle}{d \langle e^2 \rangle / dt} \approx \frac{1}{40} \left(\frac{\Omega^2 a^3}{2 G m_{pl}} \right)^2 \frac{4 m_{pl} \langle e^2 \rangle^2}{\Sigma a^2 \Omega}, \quad (6)$$

where Ω , a and e are the orbital frequencies, semimajor axes and eccentricities of the individual planetesimals. In the Stokes regime, the gas drag timescale is given by Adachi et al. (1976) as

$$t_s = \frac{2 m_{pl}}{C_D \pi r_{pl}^2 \rho_g v_g}, \quad (7)$$

where C_D is a drag coefficient of order unity, ρ_g is the local gas volume density and v_g is the headwind velocity of the gas experienced by the planetesimal. The local gas volume density is given by

$$\rho_g = \frac{\Sigma_g}{\sqrt{2\pi} h_g \exp[-z^2 / (2 h_g^2)]}, \quad (8)$$

where Σ_g is the gas surface density (taken to be 240x the solid surface density), $h_g = c_s / \Omega$ is the local gas scale height and z is the height above the disk midplane. The sound speed profile is given by $c_s = \sqrt{k_B T(r) / (\mu m_H)}$, where k_B is Boltzmann's constant, $T(r) = T_0 r^{-Q}$, $\mu = 2.34$ and m_H is the mass of a hydrogen atom. For a protoplanetary disk around a typical M star, $T_0 = 148 \text{ K}$ and $Q = 0.58$ (Andrews & Williams 2005).

Finally, the headwind velocity of the gas, due to the fact that the gas disk is pressure supported, is given by

$$v_g = v_k \left[1 - \sqrt{Q c_s^2 / v_k^2} \right], \quad (9)$$

where v_k is the local Keplerian velocity. As in section 4, the argument of perihelion ω , longitude of ascending node Ω , and mean anomaly M for the planetesimals drawn from a uniform distribution $\in [0, 2\pi)$.

5.2. Gas Drag Force

In addition to the mutual gravitational forces, a Stokes drag force from the gas disk is applied to each particle, following the prescription described in section 2.2.1 of Morishima et al. (2010). The surface density and temperature profile are identical to those used to construct the initial conditions and the cylindrical coordinate system is centered on the host star.

5.3. Timestepping Criterion

In the case of the fdHi simulation, there are nearly 1 million particles, whose orbital periods two orders of magnitude in time. Due to the very short interaction timescales near the inner edge of the disk, a fixed timestep size would require a prohibitively large number of steps to follow planetesimal growth throughout the entire disk. For this reason, we use a multi-tiered timestepping scheme, in which particles are placed onto the nearest power of two timestep based on their most

Table 2. Final Properties of Full Disk Simulations

Name	M_{PP}^a	T_{int}^b	T_{int1}^c
fdHi	100	1.5	4
fdHiShallow	100	0.5	4
fdHiSteep	100	2.5	4
fdLo	1	1.5	4

NOTE

^a Maximum protoplanet mass [M_{earth}]^b Integration time [yr]^c Rescaled integration time [yr]

recently calculated gravitational acceleration. (Mention that this scheme is used in other works with ChaNGa).

This more efficient scheme, however, introduces two additional issues related to particles interacting on different timesteps. First, momentum is not completely conserved when bodies switch timesteps. The error introduced becomes particularly severe for a particle on an eccentric Keplerian orbit, whose perihelion and aphelion distances straddle a timestep boundary. For a large collection of particles, this problem manifests itself as a V-shaped gap in the semimajor axis-eccentricity plane, which is centered on the boundary itself. To correct this problem, we introduce a second timestepping criterion, which is based on the gravitational acceleration on the particle by the central star at perihelion. Only in the case of a close encounter with another planetesimal (in which the acceleration is no longer dominated by the star) is the timestep allowed to reduce based on the original criterion.

A second issue is introduced when two particles on different timesteps undergo a collision. As in the previous case, momentum is not completely conserved because the most recent ‘kick’ steps did not happen simultaneously for these bodies. Early in the simulation, we find that runaway growth tends to trigger first at the timestep boundaries. Unfortunately, this issue carries itself forward through the embryo formation phase and protoplanets tend to form at the boundaries. To correct this issue, we ignore collisions between bodies on different timesteps early in the simulation. We find that enabling multi-timestep collisions after the maximum mass grows by a factor of 10 prevents any artifacts from forming at the timestep boundaries, while also minimizing the number of ‘skipped’ collisions².

5.4. Results

In all four simulations, the timescales for embryo formation depend on the chosen surface density profile, along with the particular location in the disk. Protoplanets form first near the inner edge of the disk, where the dynamical timescales are short. Growth proceeds in an inside-out fashion, with the outermost regions of the disk completing the protoplanet assembly phase last. This fact is not typically accounted for in planet formation simulations, and appears to be an important component to forming realistic solar system analogs (Clement et al. 2020). As with the narrow annulus simulations, we stop the integration once the mass of protoplanets in the outermost region of the disk reach a steady value. In table 2, we summarize the outcomes of the four ‘full disk’ cases.

We show the final state of the ‘fiHi’ simulation in figure 5. In the top panel, the initial (contours) and final (points) state of the simulation is shown in orbital period and eccentricity. The size of the points indicates the relative mass of the bodies. In the bottom panel, the mass of the largest bodies is shown as a function of orbital period. The solid curves indicate the isolation mass

$$M_{iso} = \left[\frac{(2\pi a^2 \Sigma \tilde{b})^3}{3M_*} \right]^{1/2}, \quad (10)$$

where \tilde{b} is the size of the feeding zone in units of Hill radii. For a body on a circular orbit $\tilde{b} = 2\sqrt{3}$, while a protoplanet formed by oligarchic growth typically has $\tilde{b} = 10$ (Kokubo & Ida 1998). The isolation mass is plotted in blue and orange for these two values of \tilde{b} , respectively.

A qualitative shift in the protoplanet and planetesimal distribution is visible at ~ 60 days. Interior to this location, there are very few remaining planetesimals and the embryos formed are noticeably more massive. Protoplanets in this region appear to closely follow the isolation mass curve for $\tilde{b} = 10$. Exterior to the boundary, the residual planetesimal population is much more numerous, and protoplanets more closely follow the $\tilde{b} = 2\sqrt{3}$ curve. This tentatively suggests that the transition between the low α and high α accretion modes seen in section 4 happens near this location.

In figure (removed), we show α (left axis) and the fraction of remaining planetesimals (right axis) as a function of orbital period. Here, the fraction of remaining planetesimals is measured by dividing the disk into 15 semimajor axis bins and using the profile function in PYNBODY to measure the total solid surface density Σ in each of those bins, and also the planetesimal surface

² In the case of fdHi, only about 20 collisions out of an eventual 900,000 are ignored.

density σ . Here, a planetesimal is defined to any body with $m < 10m_{pt}$. Exterior to 60 days in orbital period, σ/Σ sharply increases, indicating that the highly efficient accretion mode seen previously does not operate here. As can be seen from the plot, the accretion boundary roughly corresponds to $\alpha = 0.1$.

To ensure that the boundary seen near 60 days in orbital period is not simply a transient product of the inside out growth throughout the disk, we examine the time evolution of σ/Σ at multiple locations. In figure 6, the value of σ/Σ is plotted as a function of time in 10 orbital period bins. Bins interior to 60 days are indicated with a dashed line, while those exterior are indicated with a solid line. The planetesimal surface density fraction has decelerated and is approaching an asymptotic value in all cases. In the inner disk, this is driven by the near-total depletion of the planetesimal reservoir. In the outer disk, dynamical friction between the embryos and planetesimals throttles subsequent accretion.

Next, we compare the effect of varying the initial solid surface density profile on the resulting planetesimal and embryo distribution. The final orbital period-eccentricity state of the particles is shown in figure 7, with point sizes indicating the relative masses of the bodies. There is a clear trend between solid surface density at a given orbital period and the eccentricities of the remaining planetesimals. This trend is largely set by the initial conditions, as the gravitational stirring is more vigorous when bodies are packed together closely and higher eccentricities are required to produce an equilibrating aerodynamic drag force (see equations 6 and 7). Despite having significantly different masses, the planetary embryos formed in each case have remarkably similar eccentricities. This is likely due to the fact that inelastic collisions play a more significant role where the solid surface density is highest, which offsets the fact that the initial bodies started off in a dynamically hotter state.

In figure 8, we compare the masses of the resulting protoplanets and planetesimals in all four simulations to each other. Here, the masses are scaled by the isolation mass at the given orbital distance (see equation 10). In all four cases, the masses follow a similar trend: interior to about 60 days in orbital period, protoplanets grow to a factor of a few larger than M_{iso} . Exterior to this point, the protoplanet masses roughly stay near the isolation mass. Despite the drastically different solid surface density profiles used, the masses of the largest bodies in all four cases follow a similar trend with orbital period. This indicates that the highly efficient accretion mode seen at shorter orbital periods is dependent on the sizes of the individual bodies themselves, rather than

how they are distributed. The transition visible near 60 days in all cases also supports our conclusion that planetesimal accretion is largely complete everywhere in the disk.

5.5. Assembly History of Embryos

Further insight into the difference between the short vs long period accretion modes can be gained by examining the merger history of the planetary embryos. Because all collisions are directly resolved by the N-body code, a direct lineage can be traced between each embryo and a set of initial planetesimals.

We begin by investigating the ‘smoothness’ of the accretion events that give rise to each embryo. Drawing from a common technique used for cosmological simulations (citation?), we divide growth events for a given body into ‘major’ and ‘minor’ mergers. Minor events are defined as any collision involving an initial planetesimal, while major events consist of any two larger bodies. In figure 9, we show the total mass fraction gained by minor events as a function of mass for the 100 largest bodies at the end of fdHi. Blue dots represent bodies interior to the 60 day orbital period boundary, while red crosses indicate bodies exterior. For the outer bodies in the oligarchic growth region, we see a very weak trend between minor accretion mass fraction and total mass. Regardless of how much an embryo has grown, the initial mass planetesimals contribute about the same relative amount to its total mass. At shorter orbital periods, however, there is a somewhat stronger trend. The largest bodies in this region gain about an order of magnitude more of their mass fraction from major mergers, compared to the smallest bodies.

The difference in slope of the short vs longer period bodies in figure 9 indicates a difference in how the planetesimal-embryo populations interact in each region. In the long period oligarchic growth region, embryos continue to accrete planetesimals as they grow and the minor mass fraction stays mostly flat. At short period, collisions mostly occur between equal mass bodies as the embryos grow and the contribution from planetesimals becomes less significant over time. This suggests that embryo-embryo collisions are common at short period. As discussed in section 2.2, the importance of gravitational scattering is greatly reduced here. Without frequent gravitational interactions between the embryos and planetesimals, orbital repulsion (Kokubo & Ida 1998) and isolation of the embryos does not occur. As we showed in figure 8, the embryos formed in this region exceed the isolation mass.

Further evidence for the lack of gravitational scattering events can be seen in figure 10. Here, we have chosen

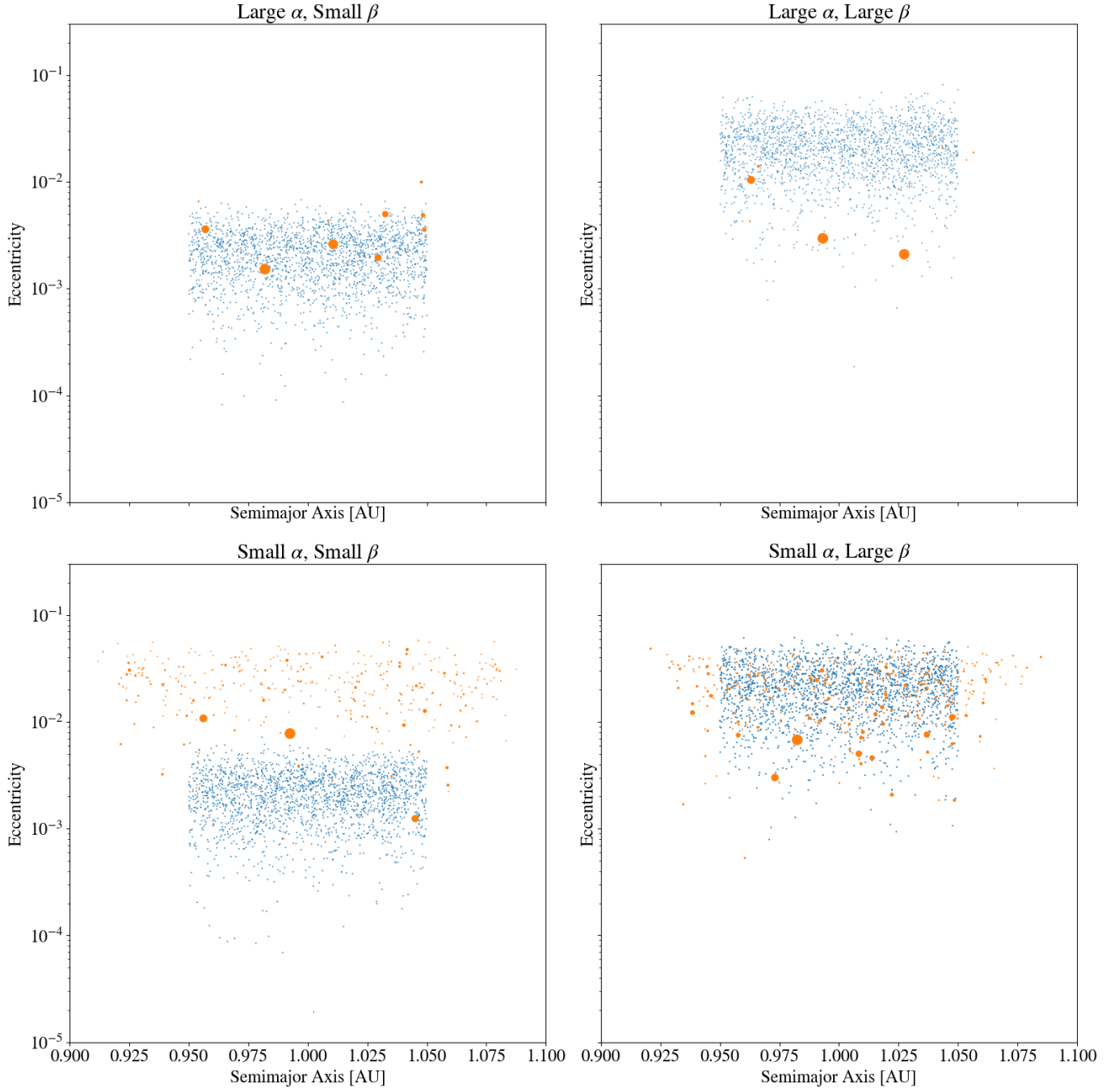


Figure 2. The initial (blue) and final (orange) states of the simulations described in section 4. Relative masses of the bodies are indicated by point size. In the case of large α , almost no residual planetesimal population remains. Regardless of the initial choice of β , the protoplanets that form attain similar eccentricities.

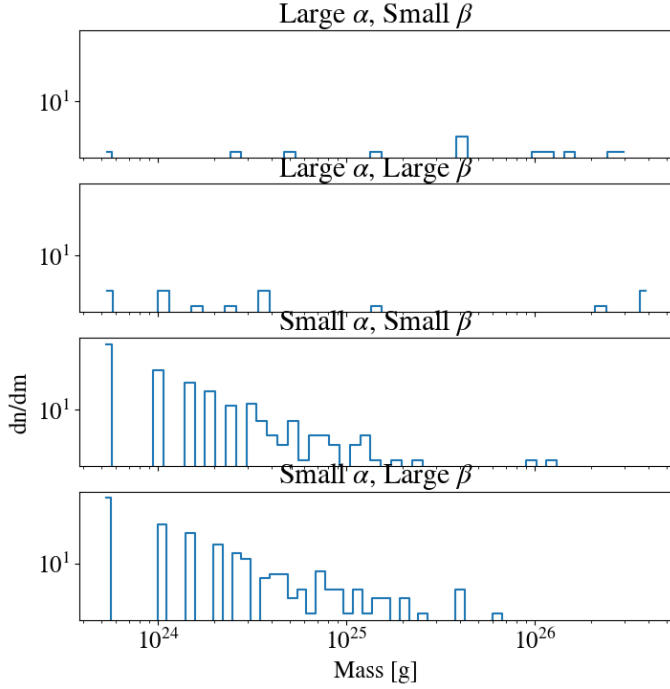


Figure 3. The final state of the mass distribution for the simulations described in section 4. For small α , a few embryos form alongside a power law tail of planetesimals. For larger values of α , the mass distribution takes on a more unimodal form. As in the previous figure, the initial choice of β does not appear to have any meaningful impact on the end result.

the 20 most massive bodies from the fdHi simulation and arranged them in order of present orbital period. The vertical black line indicates the orbital period of each embryo. The associated histogram for each body denotes where the planetesimals used to construct that embryo originated in the disk. The peaks of the histograms have all been normalized to the same value, so that the distributions only show the relative widths and locations of the feeding zones. Beyond the 60 day boundary, the ordering of the feeding zones and the embryo locations become much less consistent. This suggests that scattering events between embryos are much more common beyond this accretion mode boundary. In the inner region of the disk, close encounters between embryos often result in a merger, which allows them to grow beyond the isolation mass while only a minor alteration to their orbital period. With few close encounters resulting in a scattering event, embryos are unable to move away from their birth location.

6. SIMPLIFYING ASSUMPTIONS

6.1. Collision Cross Section

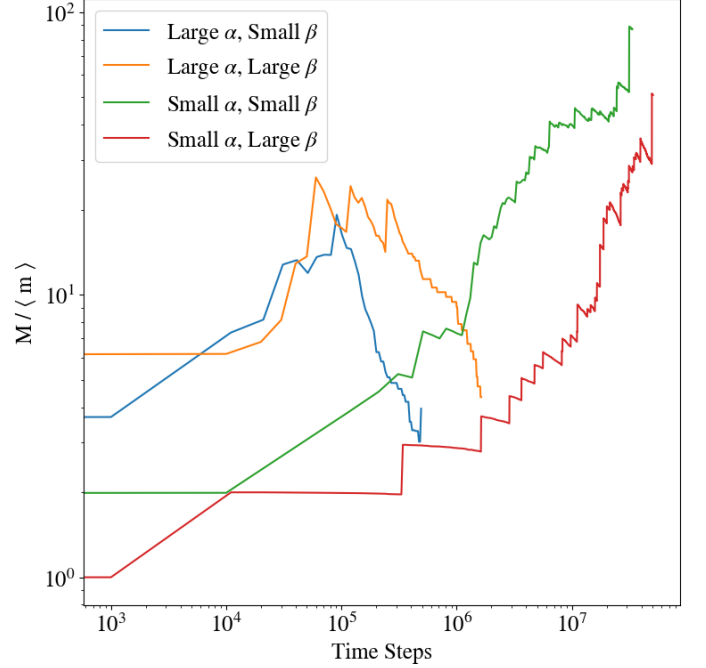


Figure 4. The evolution of the ratio between the maximum and mean mass for the four simulations presented in section 4. The runaway growth phase can be identified by a positive slope in this ratio. For all values of α , an increase in β has the effect of delaying the growth of the embryos.

In all cases shown so far, the boundary between the standard oligarchic growth and the highly-efficient short period accretion region lies around 60 days in orbital period. The mode of accretion is set entirely by the local value of α , which scales with both distance from the star and the bulk density of the planetesimals (see equation 3). The artificial inflation of the collision cross section of the particles in our simulations, which is meant to reduce the computational expense, has the side effect of reducing the bulk densities. Because $\alpha \sim \rho_{pl}^{-1/3}$, increasing the particle sizes by a factor of $f=6$ reduces the orbital period at which α has a given value by a factor of approximately 15. Therefore, one would expect the accretion boundary to lie near 5 days in orbital period for 3 g cm^{-3} bodies.

Although a simulation with $f=1$ is not computationally tractable, we can test whether the accretion boundary moves in the way we expect by modestly changing the value of f . In figure 11, we compare the fdHi simulation to a nearly identical run using $f=4$. In the top panel, the embryo masses in units of the isolation mass are shown as a function of orbital period. In the bottom panel, the value of α as a function of orbital period is shown for 3 g cm^{-3} bodies with an artificial radius enhancement of $f=1, 4$ and 6 . The horizontal dashed

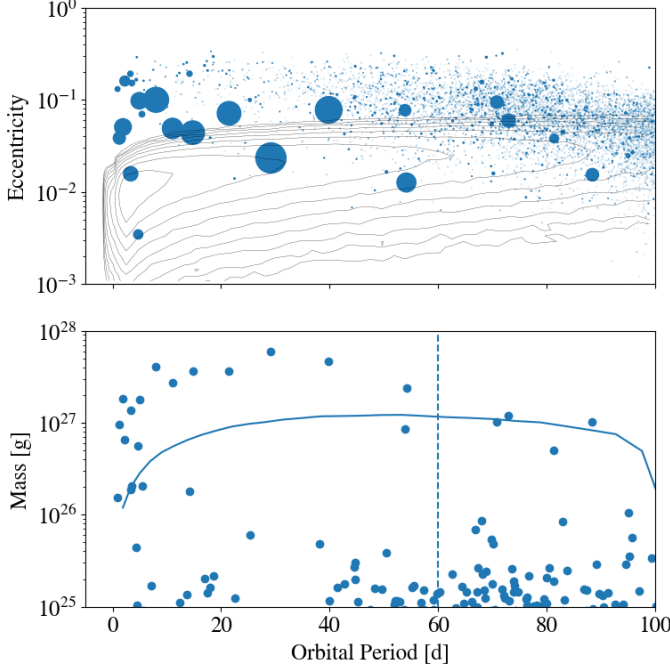


Figure 5. The final state of the fdHi simulation. In the top panel, the contours denote the initial period-eccentricity distribution of the planetesimals. Point sizes indicate the relative masses of bodies. In the bottom panel, the solid line indicates the isolation mass for $b = 2\sqrt{3}$. The vertical dashed line marks the approximate location of the accretion mode boundary. For $P_{orb} < 60$ days, the high α accretion mode produces embryos that exceed the isolation mass.

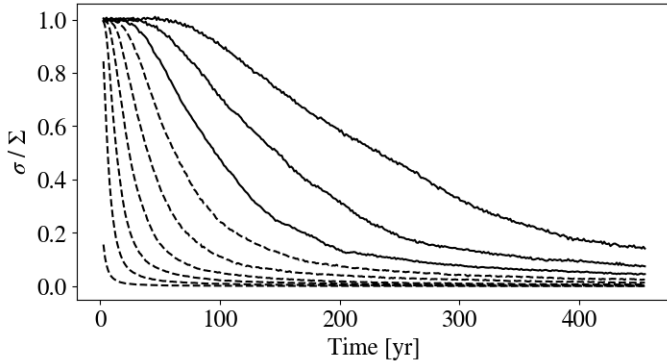


Figure 6. The time evolution of the planetesimal surface density (in units of the total solid surface density) in the fdHi simulation. Each curve represents a radial slice of the disk. The innermost region evolves the quickest, and is therefore represented by the lowest curve. The dashed lines indicate radial zones interior to the 60 day orbital period boundary.

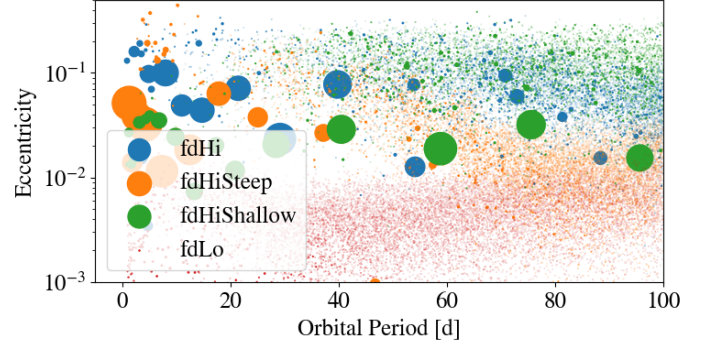


Figure 7. The final state of all simulations listed in table 2. Point sizes indicate the relative masses.

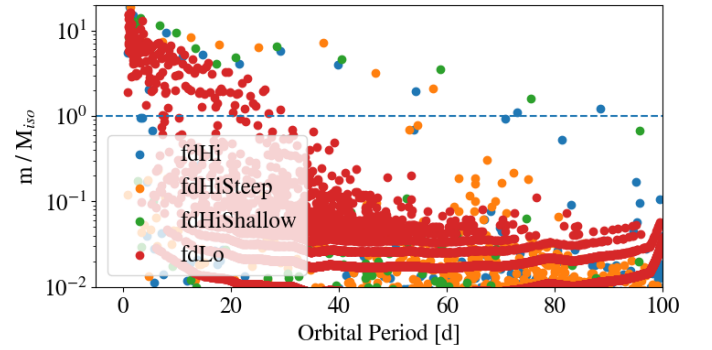


Figure 8. Masses of the remaining bodies from the simulations listed in table 2, in units of the isolation mass for $b = 2\sqrt{3}$. Despite the vastly different initial solid surface density profiles, the orbital period inside of which the embryo masses exceed the isolation mass is very consistent.

line indicates the value of α below which the accretion mode switches to oligarchic growth. Comparing the top and bottom panels, the intersection of the embryo masses and local isolation mass matches well with the orbital period at which $\alpha \sim 0.1$. Also shown by the curved dotted lines are the α curves for realistic-sized bodies with $\rho_{pl} = 1, 5$ and 10 g cm^{-3} . In all cases, the accretion boundary still lies within the part of the disk in which solids would be expected to accumulate (citation?).

6.2. Collision Model

In the simulations presented in this work, all collisions result in a complete merging of a pair of bodies with no loss of mass or momentum. Although simple to model, this assumption of perfect accretion may result in overly efficient growth, particularly at the innermost region of the disk where encounter velocities are the largest. To handle this issue properly, semianalytic collision resolution models have been developed and implemented in

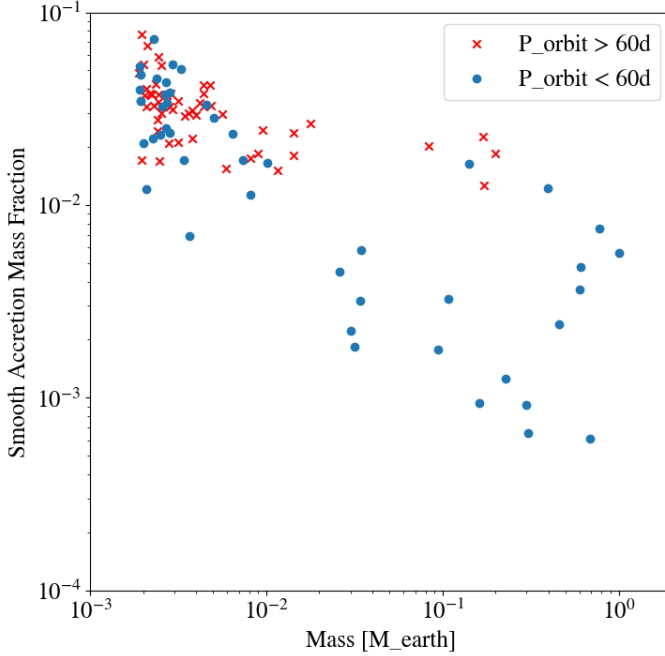


Figure 9. For the 100 most massive bodies at the end of the fdHi simulation, the fraction of their total mass attained through mergers with initial mass planetesimals (smooth accretion) as a function of total mass. Bodies that reside beyond the 60 day accretion boundary are shown with red crosses, while bodies interior to the boundary are shown with blue dots. For the short period bodies, there is a decreasing correlation between smooth accretion fraction and mass, which suggests that most growth occurs between equal mass bodies. For the longer period bodies in the oligarchic growth region, this trend is flat, indicating that accretion of planetesimals is important during all phases of evolution.

N-body codes (see (Leinhardt & Stewart 2012)). However, resolving collisional debris fragments using a direct approach as we have done with CHANGA would result in an intractably large number of particles.

To test whether a more restrictive collision model should modify our results, we present a smaller scale test using a slightly more sophisticated collision model. In this case, a collision can result in one of two outcomes: if the impact velocity is smaller than the mutual escape velocity of the colliding particles, defined as

$$v_{mut,esc} = \sqrt{\frac{G(m_1 + m_2)}{r_1 r_2}}, \quad (11)$$

where m_1, m_2 and r_1, r_2 are the masses and radii of colliding particles 1 and 2, then the bodies perfectly merge. For impact velocities larger than $v_{mut,esc}$, no mass is transferred and the bodies undergo a completely elastic bounce. Because there is no possibility of partial accretion, this model likely restricts growth more than the model used by Leinhardt & Stewart (2012). However,

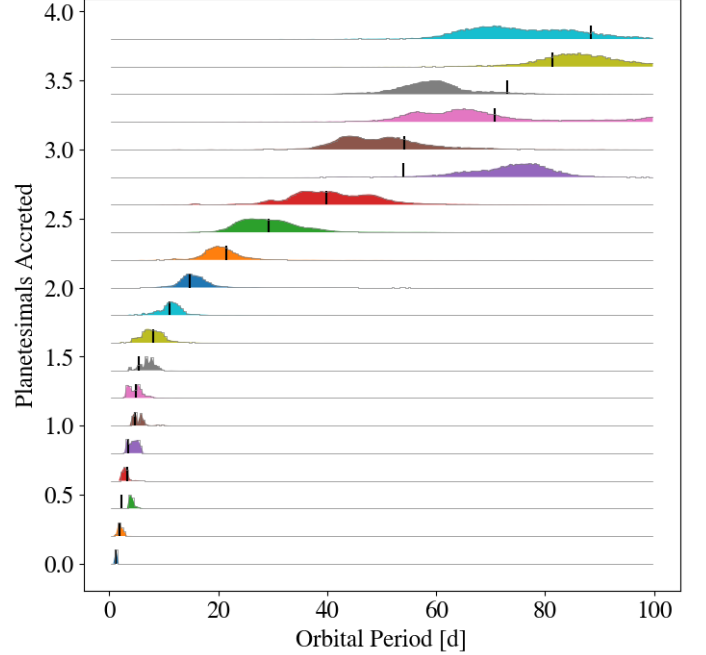


Figure 10. For the 20 most massive bodies at the end of the fdHi simulation, the relative shape of the accretion zones for each body are shown. The black hash marks indicate the present position of the body. The accretion distributions indicate the initial locations of the planetesimals that were used to assemble a body, rather than the locations at which collisions with the massive body occurred.

we will show below that the bounce-merge model does not meaningfully affect the outcome of the planetesimal accretion phase, and so a partial accretion model should do the same.

For the configuration of initial conditions we have chosen, the typical encounter velocity (defined by $v_{enc} = \langle e^2 \rangle^{1/2} v_k$, where v_k is the local Keplerian velocity) is about 25 percent larger than $v_{mut,esc}$. Because the encounter velocities follow a Gaussian distribution, there should be some small subset of collisions that still meet the merger criteria. In addition, $v_{mut,esc}$ becomes larger as the bodies grow and the merger criteria should become easier to meet as the system evolves.

In figure 12, we show the results of two versions of the fdLo simulation, one with mergers only (shown in orange) and one with the bounce-merge model (shown in green). The blue points in the top panel show the initial conditions used for both cases. Because the bounce-merge model greatly increases the number of timesteps required, we choose to model only the innermost part of the disk to reduce the computational cost. Although the bounce-merge simulation takes much longer to reach the same phase of evolution, the resulting orbits and masses

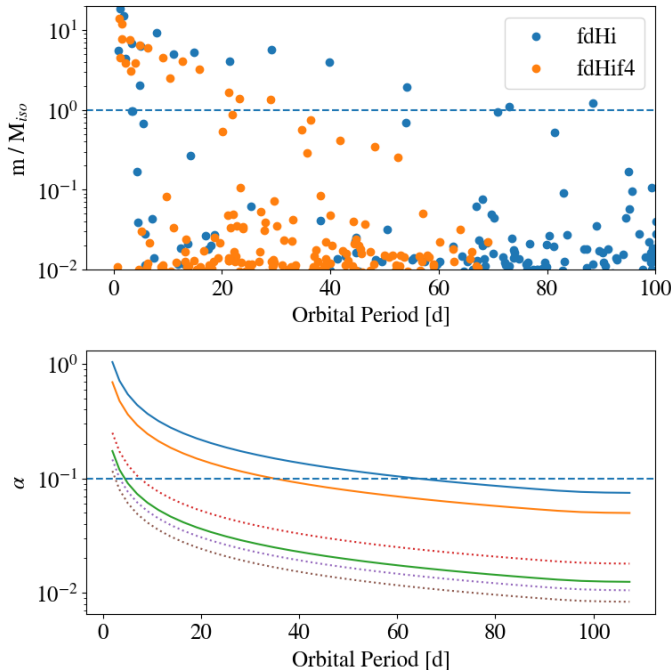


Figure 11. In the top panel, we show the final masses of the bodies from the fdHi and fdHif4 simulations in units of the isolation mass for $b = 2\sqrt{3}$. The bottom panel shows the variation of α with orbital period for the bodies used in each case (solid curves). The orbital period at which $\alpha \simeq 0.1$ matches well with the intersection of the embryo mass distribution and isolation mass. The dotted curves in the bottom panel show the values of alpha for realistic-sized planetesimals with $\rho = 1, 3, 5$ and 10 g cm^{-3} . (need to fix the green curve)

of the embryos are indistinguishable from the merger-only case.

To investigate the differences between the two collision models early in the simulations, we show the time evolution of the ratio between the maximum and mean mass in figure 13. In both cases, this ratio grows at early times, which indicates that runaway growth still operates, regardless of the collision model used. In the bounce-merge case, the mass ratio peaks at a higher value, while also undergoing a longer runaway growth phase. This suggests that the mass distribution becomes much less unimodal during this growth process, but as figure 12 shows, this does not affect the resulting embryos or allow for a residual planetesimal population.

6.3. Type I Migration

What is the migration timescale for the embryos to move to the inner edge of the disk? Maybe this section isn't terribly important and should be excluded?

7. SUMMARY AND DISCUSSION

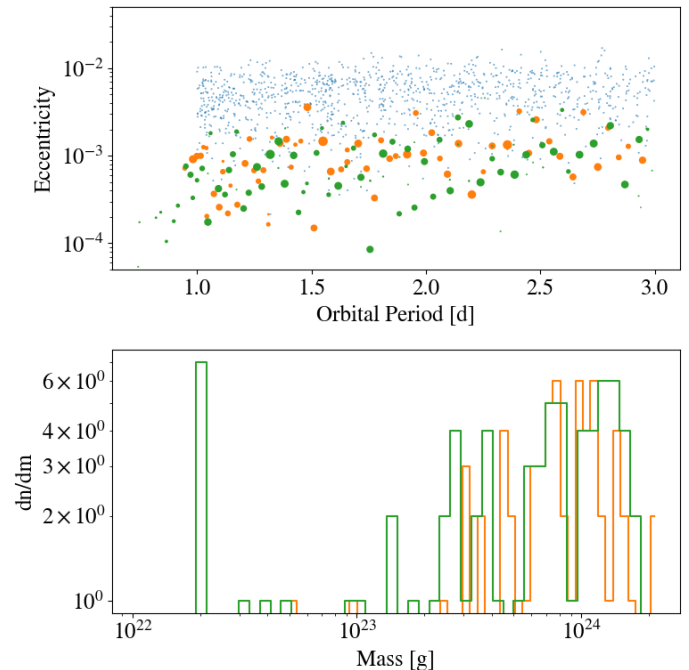


Figure 12. A comparison between the innermost regions of the fdLo (orange) simulation, and a second version using a bounce-merge collision model (green). In the top panel, the period-eccentricity state of the particles is shown, with marker sizes indicating relative mass. The blue points represent the initial state of the simulations. The bottom panel compares the final masses of the bodies.

In this work, we have demonstrated that planetary embryo formation operates in two distinct modes in a planet-forming disk. In the first mode, gravitational feedback from the growing embryos heats the remaining planetesimals and results in a dynamically cold population of embryos with a significant amount of residual planetesimals. This corresponds to the ‘oligarchic growth’ case revealed by (Kokubo & Ida 1998). In the second mode, the gravitational feedback does not operate, embryos quickly sweep up all planetesimals, and grow about twice as large as is predicted by oligarchic growth. The distinction between these modes is determined by ratio between the physical size of the bodies and their Hill radius.

We have demonstrated the outcome of both accretion modes through a low resolution parameter study. The initial planetesimal distribution can be described in terms of two dimensionless constants, α and β , which describe the ratio between the physical radius of the planetesimals and the Hill (r_h) and gravitational (r_g) radii, respectively. For a fixed planetesimal mass and radius, α scales with the orbital period and β scales with the level of dynamical excitation of the disk. We showed that

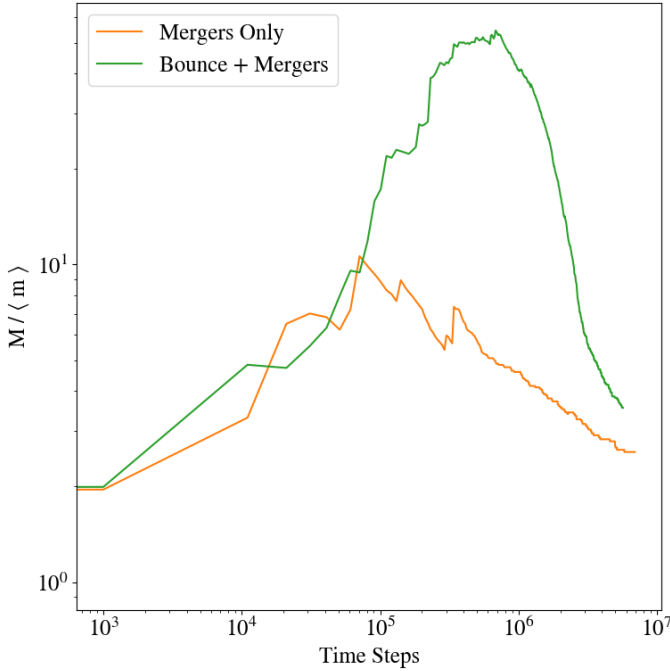


Figure 13. The evolution of the ratio between the maximum and mean mass of the simulations shown in figure 12. In both cases, the system first evolves through a phase of runaway growth, before the massive bodies consume the smaller bodies, driving down the mean mass. With the bounce-merge model, the mass ratio decreases later because not all collisions result in growth.

$\alpha \ll 1$ leads to oligarchic growth, while a non-negligible α produces this new non-oligarchic growth mode. We find that the resulting mass distribution, along with the final eccentricities of the embryos and residual planetesimals, ends up the same, regardless of the initial value of β .

So long as the density of the bodies does not significantly change as their mass distribution evolves, this ratio, and therefore the boundary between these accretion modes is set entirely by the distance from the star. Because both the physical and Hill radius of the bodies grows as $M^{1/3}$, the boundary between growth remains at a fixed location in the disk during the planetesimal accretion process.

We have verified this fact by testing the outcome of the planetesimal accretion process for a variety of solid surface density profiles. Although altering the surface density does affect the resulting masses of the embryos, the location of the boundary separating the growth modes is remarkably similar between all of our simulations. We have verified this by comparing the resulting embryo masses to the isolation mass, in addition to highlighting

qualitative differences in the accretion history of embryos on both sides of the boundary.

Lastly, we quantified the way in which our use of perfect accretion and an inflated collision cross section, both meant to make the simulations more computationally tractable, affect the non-oligarchic growth mode and the location of the accretion boundary. We showed that although the use of perfect accretion speeds up the growth of the embryos, it does not affect the masses or orbital properties of the resulting bodies. Because the inflated collision cross sections artificially reduce the density of the planetesimals, this shortcut does shift the accretion boundary outward. However, it moves in a predictable fashion and we verified this by running an extra simulation with a modestly smaller collision cross section. In a real planet-forming disk, one would expect this boundary to lie somewhere between 2 and 10 days, depending on the composition of the planetesimals.

To date, there have been no other studies of planetesimal accretion with such a large value of α . However, a value of $\alpha = 1$ corresponds to the Roche limit of a three-body system, and so one might wonder this high- α accretion mode might be relevant for a circumplanetary system. There is a small collection of previous works which use N-body methods to examine in-situ satellitesimal accretion (Ida et al. 1997; Richardson et al. 2000; Ida et al. 2020). Ida et al. (1997) was able to form 1-2 large moon just exterior to the Roche limit, depending on the extent of the disk with very little satellitesimal material left over. The widest disk they modeled extended out to $\alpha = 0.5$. Qualitatively, this result is very similar to the short period planetesimal accretion mode observed in our simulations. Ida et al. (2020) modeled a much wider satellitesimal disk, which extends out to about $\alpha \approx 0.05$. Inside to the $\alpha = 0.1$ accretion boundary (which lies near $15R_U$ in figure 1 of Ida et al. (2020)), bodies grow beyond the isolation mass, while the opposite is true on the other side of the boundary. In addition, a residual population of satellitesimals is still present beyond the boundary, which suggests that oligarchic growth is indeed operating on the far side.

Presently, the implications that this non-oligarchic accretion mode has for the formation of short-period terrestrial planets, and whether the accretion boundary would leave any lasting imprint on the final orbital architecture, is unclear. One point that our results do highlight is that the initial conditions used for most late stage planet formation simulations are overly simplistic. Clement et al. (2020) recently simulated planetesimal accretion in a disk extending from the orbit of Mercury to the asteroid belt and found that the disk never reaches a state in which equally-spaced, isolation mass embryos

are present everywhere simultaneously. Instead, different annuli reach a ‘giant impact’ phase at different times, preventing the onset of a global instability throughout the entire disk, as is common in classic terrestrial planet formation models (Chambers & Wetherill 2001; Raymond et al. 2009).

To connect these accretion modes to the final orbital architecture, and to ultimately determine what implica-

tions an in situ formation model has for the growth of STIPs, we will continue to evolve the final simulation snapshots presented here with a hybrid symplectic integrator. The final distribution of planets formed, along with composition predictions generated by applying cosmochemical models to our initial planetesimal distributions and propagating compositions through the merger trees, will be examined in a follow-up paper.

REFERENCES

- Adachi, I., Hayashi, C., & Nakazawa, K. 1976, *Progress of Theoretical Physics*, 56, 1756, doi: [10.1143/PTP.56.1756](https://doi.org/10.1143/PTP.56.1756)
- Alibert, Y., Mordasini, C., & Benz, W. 2011, *A&A*, 526, A63, doi: [10.1051/0004-6361/201014760](https://doi.org/10.1051/0004-6361/201014760)
- Andrews, S. M., & Williams, J. P. 2005, *ApJ*, 631, 1134, doi: [10.1086/432712](https://doi.org/10.1086/432712)
- Barnes, R., Quinn, T. R., Lissauer, J. J., & Richardson, D. C. 2009, *Icarus*, 203, 626, doi: [10.1016/j.icarus.2009.03.042](https://doi.org/10.1016/j.icarus.2009.03.042)
- Chambers, J. E., & Wetherill, G. W. 1998, *Icarus*, 136, 304, doi: [10.1006/icar.1998.6007](https://doi.org/10.1006/icar.1998.6007)
- . 2001, *M&PS*, 36, 381, doi: [10.1111/j.1945-5100.2001.tb01881.x](https://doi.org/10.1111/j.1945-5100.2001.tb01881.x)
- Clement, M. S., Kaib, N. A., & Chambers, J. E. 2020, *PSJ*, 1, 18, doi: [10.3847/PSJ/ab91aa](https://doi.org/10.3847/PSJ/ab91aa)
- Fischer, R. A., & Ciesla, F. J. 2014, *Earth and Planetary Science Letters*, 392, 28, doi: [10.1016/j.epsl.2014.02.011](https://doi.org/10.1016/j.epsl.2014.02.011)
- Hansen, B. M. S., & Murray, N. 2012, *ApJ*, 751, 158, doi: [10.1088/0004-637X/751/2/158](https://doi.org/10.1088/0004-637X/751/2/158)
- Hayashi, C. 1981, *Progress of Theoretical Physics Supplement*, 70, 35, doi: [10.1143/PTPS.70.35](https://doi.org/10.1143/PTPS.70.35)
- Ida, S. 1990, *Icarus*, 88, 129, doi: [10.1016/0019-1035\(90\)90182-9](https://doi.org/10.1016/0019-1035(90)90182-9)
- Ida, S., Canup, R. M., & Stewart, G. R. 1997, *Nature*, 389, 353, doi: [10.1038/38669](https://doi.org/10.1038/38669)
- Ida, S., Kokubo, E., & Makino, J. 1993, *MNRAS*, 263, 875, doi: [10.1093/mnras/263.4.875](https://doi.org/10.1093/mnras/263.4.875)
- Ida, S., & Lin, D. N. C. 2004, *ApJ*, 604, 388, doi: [10.1086/381724](https://doi.org/10.1086/381724)
- Ida, S., & Makino, J. 1993, *Icarus*, 106, 210, doi: [10.1006/icar.1993.1167](https://doi.org/10.1006/icar.1993.1167)
- Ida, S., Ueta, S., Sasaki, T., & Ishizawa, Y. 2020, *Nature Astronomy*, 4, 880, doi: [10.1038/s41550-020-1049-8](https://doi.org/10.1038/s41550-020-1049-8)
- Jetley, P., Gioachin, F., Mendes, C. Kale, L., & Quinn, T. 2008, *Proceedings of IEEE International Parallel and Distributed Processing Symposium*
- Kokubo, E., & Ida, S. 1996, *Icarus*, 123, 180, doi: [10.1006/icar.1996.0148](https://doi.org/10.1006/icar.1996.0148)
- . 1998, *Icarus*, 131, 171, doi: [10.1006/icar.1997.5840](https://doi.org/10.1006/icar.1997.5840)
- . 2000, *Icarus*, 143, 15, doi: [10.1006/icar.1999.6237](https://doi.org/10.1006/icar.1999.6237)
- Leinhardt, Z. M., & Stewart, S. T. 2012, *ApJ*, 745, 79, doi: [10.1088/0004-637X/745/1/79](https://doi.org/10.1088/0004-637X/745/1/79)
- Levison, H. F., Morbidelli, A., Tsiganis, K., Nesvorný, D., & Gomes, R. 2011, *AJ*, 142, 152, doi: [10.1088/0004-6256/142/5/152](https://doi.org/10.1088/0004-6256/142/5/152)
- Menon, H., Wesolowski, L., & Zheng, G. e. a. 2015, *Computational Astrophysics and Cosmology*, 2, 1
- Morishima, R., Stadel, J., & Moore, B. 2010, *Icarus*, 207, 517, doi: [10.1016/j.icarus.2009.11.038](https://doi.org/10.1016/j.icarus.2009.11.038)
- Nesvorný, D. 2011, *ApJL*, 742, L22, doi: [10.1088/2041-8205/742/2/L22](https://doi.org/10.1088/2041-8205/742/2/L22)
- Raymond, S. N., & Izidoro, A. 2017, *Science Advances*, 3, e1701138, doi: [10.1126/sciadv.1701138](https://doi.org/10.1126/sciadv.1701138)
- Raymond, S. N., O’Brien, D. P., Morbidelli, A., & Kaib, N. A. 2009, *Icarus*, 203, 644, doi: [10.1016/j.icarus.2009.05.016](https://doi.org/10.1016/j.icarus.2009.05.016)
- Raymond, S. N., Quinn, T., & Lunine, J. I. 2006, *Icarus*, 183, 265, doi: [10.1016/j.icarus.2006.03.011](https://doi.org/10.1016/j.icarus.2006.03.011)
- Richardson, D. C. 1994, *MNRAS*, 269, 493, doi: [10.1093/mnras/269.2.493](https://doi.org/10.1093/mnras/269.2.493)
- Richardson, D. C., Quinn, T., Stadel, J., & Lake, G. 2000, *Icarus*, 143, 45, doi: [10.1006/icar.1999.6243](https://doi.org/10.1006/icar.1999.6243)
- Safronov, V. S. 1969, *Evoliutsiia doplanetnogo oblaka*.
- Tsiganis, K., Gomes, R., Morbidelli, A., & Levison, H. F. 2005, *Nature*, 435, 459, doi: [10.1038/nature03539](https://doi.org/10.1038/nature03539)
- Wallace, S. C., & Quinn, T. R. 2019, *MNRAS*, 489, 2159, doi: [10.1093/mnras/stz2284](https://doi.org/10.1093/mnras/stz2284)
- Walsh, K. J., Morbidelli, A., Raymond, S. N., O’Brien, D. P., & Mandell, A. M. 2011, *Nature*, 475, 206, doi: [10.1038/nature10201](https://doi.org/10.1038/nature10201)
- Weidenschilling, S. J. 1989, *Icarus*, 80, 179, doi: [10.1016/0019-1035\(89\)90166-8](https://doi.org/10.1016/0019-1035(89)90166-8)
- Wetherill, G. W., & Stewart, G. R. 1989, *Icarus*, 77, 330, doi: [10.1016/0019-1035\(89\)90093-6](https://doi.org/10.1016/0019-1035(89)90093-6)